Design and Implementation of PID Adaptation Mechanism for MRAS-Based Speed Estimation of Induction Machine

Fnaiech, M. A.; Trabelsi, M.; Al-Khazraji, A.; Taleb, M.; Vahedi, H.

DOI
10.1109/OJIES.2025.3587055

Publication date
2025

Document Version
Final published version

Published in
IEEE Open Journal of the Industrial Electronics Society

IEEE Open Journal of the
Industrial Electronics Society

Received 31 May 2025; revised 30 June 2025; accepted 1 July 2025. Date of publication 10 July 2025;
date of current version 23 July 2025. The review of this article was arranged by Associate Editor Giampaolo Buticchi.

Digital Object Identifier 10.1109/OJIES.2025.3587055

Design and Implementation of PID Adaptation Mechanism for MRAS-Based Speed Estimation of Induction Machine

MOHAMED AMINE FNAIECH [1] (Senior Member, IEEE), MOHAMED TRABELSI [2] (Senior Member, IEEE), AYMAN AL-KHAZRAJI[1], MAAMAR TALEB[1], AND HANI VAHEDI [3] (Senior Member, IEEE)

[1]College of Engineering, Electrical Engineering Department, University of Bahrain, Sakhir 32038, Bahrain
[2]Electronics and Communications Engineering Department, Kuwait College of Science and Technology, 27235 Kuwait City, Kuwait
[3]Department of Electrical Engineering, Mathematics, and Computer Science, Delft University of Technology, 2628 CD Delft, The Netherlands

CORRESPONDING AUTHOR: MOHAMED AMINE FNAIECH (e-mail: mfnaiech@uob.edu.bh).

ABSTRACT This article proposes the use of a proportional–integral–derivative (PID) controller as an adaptive mechanism within the framework of the model reference adaptive system-based rotor flux (MRASF) for accurate rotor speed estimation in induction motors. The controller is designed to impose specific dynamic behaviors and performance criteria, addressing the sensitivity of MRASF dynamics to slip speed. To achieve this, a full-order transfer function of the MRASF is employed to systematically derive the PID parameters using compensation and pole placement techniques. The proposed control strategy ensures that the estimated rotor speed closely follows the desired performance across various operating conditions. The effectiveness of the MRASF–PID design is validated through both simulation and experimental testing under open-loop voltage/frequency control of the induction machine, confirming the successful realization of the targeted dynamic and steady-state performance.

INDEX TERMS Proportional–integral–derivative (PID) controller (CN), model reference adaptive system (MRAS), speed estimation, induction machines (IMs), closed-loop control system.

NOMENCLATURE

R_r	Rotor resistance.
L_r	Rotor inductance.
L_s	Stator inductance.
L_m	Main inductance.
$\lambda = \frac{R_r}{L_r}$	Inverse of rotor time constant.
$v_{s\alpha}, v_{s\beta}$	α-β stator voltage components.
$i_{s\alpha}, i_{s\beta}$	α-β stator current components.
$\psi_{r\alpha}, \psi_{r\beta}$	α-β rotor flux components.
ω_r	Rotor electrical angular speed.
s	Laplace variable.
ω_{sl}	Slip angular speed.
Ω	Rotor mechanical shaft speed.
$.^*$	Desired value.
$\hat{.}$	Estimated value.
CLTF	Closed-loop transfer function.
DCLTF	Desired closed-loop transfer function.
CN	Controller.
IM	Induction machine.
MRASF	Model reference adaptive system-based rotor flux.
PID	Proportional–integral–derivative.
RT	Rise-time.
ST	Settling-time.
V/F	Voltage/frequency control.
r/min	Revolution-per-minute.

I. INTRODUCTION

The MRASF represents a well-established and dependable methodology for estimating the operational velocity of IMs [1]. This system endeavors to minimize the discrepancy between a reference model of rotor flux and an adaptive model of rotor flux through a control mechanism termed an adaptation CN [2], [3], [4]. The mathematical representation of MRASF yields a transfer function framework, thereby providing a systematic basis for the design of CN that guarantee precise rotor speed estimation while adhering to

defined performance standards [5]. In its nascent implementations, MRASF predominantly utilized proportional–integral (PI) CN, with parameters derived from a reduced-order transfer function of MRASF [6]. By disregarding slip speed and presuming that rotor speed closely approximates synchronous speed, the system dynamics were simplified to a first-order transfer function [7].

Despite its notable accomplishments, the inherent simplification present in the architecture of the PI CN for MRASF has resulted in discrepancies across diverse operational velocities and load conditions. To mitigate these limitations, substantial progress has been achieved in the efficacy of MRASF within the framework of sensorless vector control (SVC). For instance, at low and zero velocities, the application of the predictive model reference adaptive system (MRAS) has been utilized, incorporating predictive algorithms to improve dynamic responsiveness [8], [9]. In contexts characterized by high-speed operations, the implementation of a sliding-mode-based MRAS provides enhanced robustness through the integration of a sliding-mode observer with the conventional MRASF [7], [10], [11], [12], [13], [14]. Moreover, the introduction of neural network-based MRAS approaches has been proposed as an alternative to traditional voltage models, employing machine learning estimators that exhibit effectiveness in low-frequency and low-speed settings [15], [16]. Furthermore, adaptive high-gain MRAS techniques have demonstrated potential in ultra-low-speed and regenerative mode operations by integrating high-gain observers within MRASF, thus ensuring stability and precision under critical operational conditions [17]. While all the previously mentioned studies have examined the effectiveness of sensorless closed-loop control of the IM functioning in a steady state, the assessment of the MRASF in these analyses is regarded as rudimentary and imprecise due to the existing overlap among the control loops. In contrast, this article focuses exclusively on the dynamics and performance of the MRASF, with an evaluation conducted under open-loop control of the IM, thereby eliminating any overlap.

This article proposes an innovative PID CN as the adaptation mechanism for MRASF, with the objective of imposing the requisite dynamics for accurate rotor speed estimation. The PID CN remains widely favored in industrial contexts due to its simplicity, stability, and efficacy in accommodating diverse operational conditions [18]. To ensure a precise performance assessment of the proposed MRASF–PID, the estimated speed must not be utilized within a control loop. Instead, performance evaluations should be executed with the IM functioning under free mechanical dynamics. Given that validating MRASF performance necessitates covering a comprehensive range of rotor speeds, the implementation of an open-loop V/F control for the IM presents a unique strategy to fulfill this objective.

The operational efficacy of the PID CN is frequently constrained to specific operating points [19], [20]. This limitation necessitates scrupulous calibration when implemented

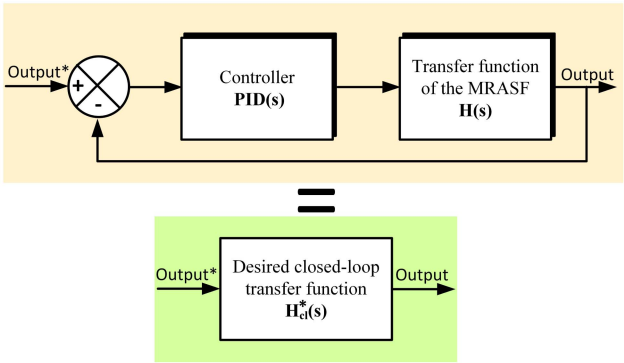

FIGURE 1. Compensation and poles placement method for MRASF estimator.

in systems defined by unknown or time-varying dynamics [18], [21]. A variety of PID tuning methodologies have been proposed to enhance adaptability and effectiveness. Techniques, such as feedback relay tuning [22], frequency-domain methodologies [23], [24], extremum-seeking algorithms [25], and iterative feedback tuning [26], have been thoroughly examined. Furthermore, strategies encompassing cross-correlation analysis, Newton–Raphson optimization, and model predictive control have been developed to improve PID performance within dynamic contexts [27], [28], [29]. Among these techniques, compensation and pole placement methodologies have exhibited notable effectiveness in refining PID parameters when the transfer function of the system varies with changing operating conditions [18].

In this manuscript, an innovative PID-based adaptation mechanism for MRASF is introduced, employing a full-order transfer function that accommodates variations in slip speed. The PID parameters are determined utilizing compensation and pole placement strategies by equating the closed-loop transfer function [desired closed-loop transfer function (DCLTF)] noted H_{cl}, of the MRASF-PID CN with a predetermined DCLTF noted H^*_{cl} that delineates the target system dynamics and performance metrics (Fig. 1)

$$\text{PID}(s) = \frac{H^*_{\text{cl}}(s)}{H(s) - H(s)H^*_{\text{cl}}(s)}.$$

Consequently, the PID parameters are explicitly derived as functions of the MRASF model parameters, the desired performance criteria, and the slip speed. To realize the targeted performance under both transient and steady-state conditions, it is imperative to fine-tune the PID parameters for each specific speed level. The proposed PID-MRASF approach is especially relevant for applications requiring reliable sensorless control under dynamic conditions, such as electric vehicles, renewable energy systems, and robotics.

The rest of this article is organized as follows. Section II delineates the mathematical modeling of MRASF predicated on the differential equations that govern the rotor flux of the IM. Section III elucidates the design methodology for the

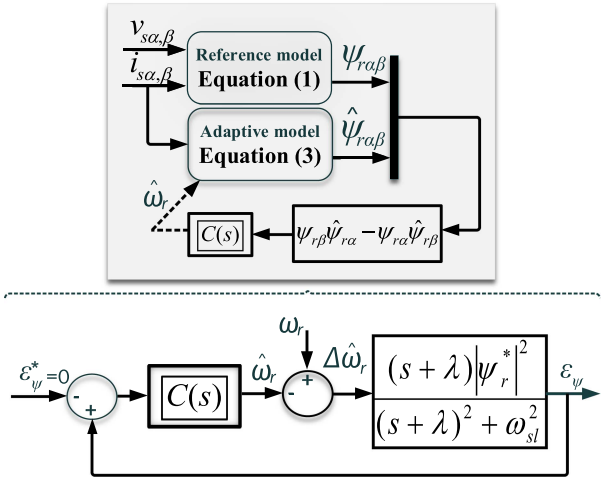

FIGURE 2. Design and the mathematical concept of MRASF estimator.

proposed PID CN, leveraging the full-order transfer function of MRASF, and examines simulation results that validate the proposed approach. Section IV elaborates on experimental validation and assesses the performance of the MRASF-based PID CN. Finally, Section V encapsulates the principal findings and proposes avenues for future research.

II. MATHEMATICAL DESIGN OF FLUX-BASED MRAS ESTIMATOR

A plethora of estimator algorithms pertinent to IM has been delineated within the existing body of literature [30]. This manuscript aims to elucidate the theoretical foundations and analytical considerations associated with the formulation of the proposed PID CN applicable to the full-order transfer function of the MRASF estimator. The MRASF estimator employed within the context of IM is predicated upon two distinct sets of differential equations requisite for the computation of rotor flux. One of these equations encapsulates the variable subject to estimation—specifically, the rotor speed (ω_r). The equation that is devoid of the estimated rotor speed is designated as the reference model (1), whereas the equation that incorporates the rotor speed is referred to as the adaptive model (2). The disparity between the output values generated by these two models is utilized to devise a suitable adaptation mechanism that produces the estimated rotor speed ($\hat{\omega}_r$) for the adaptive model [4], [31], [32]

$$\psi_{r\alpha,\beta} = \frac{L_r}{L_m}\left\{\frac{(v_{s\alpha,\beta} - R_s i_{s\alpha,\beta})}{s} - L_s\sigma i_{s\alpha,\beta}\right\} \tag{1}$$

$$\begin{cases}\psi_{r\alpha} = \frac{1}{s}\left(-\lambda\psi_{r\alpha} - \omega_r\psi_{r\beta} + \lambda L_m i_{s\alpha}\right)\\ \psi_{r\beta} = \frac{1}{s}\left(-\lambda\psi_{r\beta} + \omega_r\psi_{r\alpha} + \lambda L_m i_{s\beta}\right).\end{cases} \tag{2}$$

Fig. 2 shows the design and mathematical theory of the MRASF estimator applied for an IM.

To explain the mathematical theory of the MRASF estimator, the estimated rotor speed should be considered first in the adaptive model. Hence, (2) can be rewritten as follows:

$$\begin{cases}\hat{\psi}_{r\alpha} = \frac{1}{s}\left(-\lambda\hat{\psi}_{r\alpha} - \hat{\omega}_r\hat{\psi}_{r\beta} + \lambda L_m i_{s\alpha}\right)\\ \hat{\psi}_{r\beta} = \frac{1}{s}\left(-\lambda\hat{\psi}_{r\beta} + \hat{\omega}_r\hat{\psi}_{r\alpha} + \lambda L_m i_{s\beta}\right).\end{cases} \tag{3}$$

The performance and dynamics of the MRASF were discussed in [7]. It was also proven that the transfer function given by (4) links the norm of the flux error to the speed error. It can be expressed as follows:

$$\frac{\varepsilon_\psi}{\Delta\hat{\omega}_r} = \frac{(s+\lambda)\psi^{*2}_r}{(s+\lambda)^2 + \omega^2_{sl}} \tag{4}$$

where $\varepsilon_\psi = \psi_{r\beta}\hat{\psi}_{r\alpha} - \hat{\psi}_{r\beta}\psi_{r\alpha}$ and $\Delta\hat{\omega}_r = \omega_r - \hat{\omega}_r$.

The static gain of the transfer function presented in (4) is approximately equal to 1. Taking into account Popov hyperstability criteria which implies that if the norm of the flux error reaches zero ($\varepsilon_\psi \to 0$), then the speed error reaches zero ($\Delta\hat{\omega}_r \to 0$) and consequently $\hat{\omega}_r$ reaches ω_r.

For the unknown signal ω_r, the goal of the closed-loop control system is to control the norm of the flux error ε_ψ to follow its desired zero value ε^*_ψ. The CN used in the closed-loop generates the desired $\hat{\omega}_r$ which ensures that $\Delta\hat{\omega}_r = 0$. Thus, the estimated rotor speed is calculated as follows:

$$\hat{\omega}_r = C(s)\varepsilon_\psi \tag{5}$$

where $C(s)$ is the CN used for controlling the norm of flux error. It is designed based on the following transfer function which is deduced from the (4):

$$\frac{\varepsilon_\psi}{\hat{\omega}_r} = \frac{(s+\lambda)\psi^{*2}_r}{(s+\lambda)^2 + \omega^2_{sl}}. \tag{6}$$

Despite the prevalent misconception that ω_{sl} is equivalent to zero, prior scholarly investigations underscore the importance of the MRASF estimator and advocate for its implementation in the tuning of the PI CN. This methodology has exhibited encouraging outcomes, particularly in high-velocity applications [1], [5]. Under this premise, the transfer function delineated in (6) can be reduced to a first-order transfer function

$$\frac{\varepsilon_\psi}{\hat{\omega}_r} = \frac{\psi^{*2}_r}{(s+\lambda)}. \tag{7}$$

Consequently, the parameters of the PI CN can be determined using the strategic pole placement method applied to the CLTF

$$PI(s) = K_p + \frac{K_i}{s} \tag{8}$$

where $K_p = \frac{1}{\tau\psi^{*2}_r}$, $K_i = \frac{\lambda}{\tau\psi^{*2}_r}$, and τ is the desired constant time.

MRASF has been linked to nonlinear and intelligent algorithms, such as sliding mode control and fuzzy control [7], [10], [11]. Although these closed-loop algorithms have demonstrated strong performance, achieving precise dynamics in MRASF remains challenging.

Sliding mode control is a nonlinear technique that adjusts its structure based on the position of the system's state

variables in the phase plane. While it shows impressive robustness according to the Lyapunov criterion, its convergence dynamics are unpredictable, often relying on trial-and-error to determine the slope of the sliding surface and the state feedback gain [7], [10].

Fuzzy logic control, on the other hand, is a model-free intelligent control system that uses error and the rate of change of error as input signals. The input and output signals in fuzzy control must be multiplied by adjustment coefficients to optimize system performance. Like sliding mode control, the convergence dynamics of the fuzzy CN are also unpredictable and depend on trial-and-error methods to select these coefficients [11].

The primary objective of this research is to develop CN that can impose a precise dynamic on the MRASF. Consequently, this manuscript argues that ω_{sl} is not equal to zero. The design's theoretical framework will incorporate the second-order transfer function presented in (6). The next section will concentrate on formulating the proposed CN, which is a PID CN for the complete second-order transfer function of the MRASF.

III. PID DESIGN FOR MRAS ADAPTATION MECHANISM

The initial section will delineate the proposed design methodology for the PID CN, employing the comprehensive transfer function of the MRASF. The subsequent section will emphasize the simulation process to evaluate the performance attained in relation to the predefined objectives.

A. DESIGN THEORY

The mathematical modeling of the process constitutes a fundamental component in the design of a precise CN aimed at optimizing the entirety of the control system. Indeed, the presence of an open-loop transfer function, a CN, and negative feedback establishes a straightforward and effective framework that is advantageous for initiating the design process. Consequently, the computation of the CLTF, denoted as H_{cl}, is regarded as a trivial endeavor. The delineation of the desired closed-loop performance is achieved by selecting the DCLTF, denoted as H^*_{cl}. Ultimately, the requisite CN is ascertained by equating the CLTF (H_{cl}) with the DCLTF (H^*_{cl}).

The transfer function delineated previously in (6) shall be employed in all ensuing design phases. This transfer function encompasses a stable zero that may be mitigated within the control apparatus. The CN will be conceived in accordance with the amended transfer function postcompensation, whilst taking into account the requisite closed-loop performance criteria.

The CLTF H_{cl} of the bloc diagram presented in Fig. 3, can be written as follows:

$$H_{\text{cl}}(\text{s}) = \frac{\text{CN(s)}\psi_r^{*2}}{(s+\lambda)^2 + \omega_{sl}^2 + \text{CN(s)}\psi_r^{*2}} \tag{9}$$

where CN(s) is the CN to be designed for achieving the desired performances of MRASF.

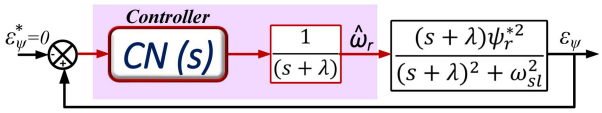

FIGURE 3. Structure of control for MRASF estimator.

The DCLTF H^*_{cl} is characterized by a unity static gain and real negative poles, is chosen as

$$H^*_{\text{cl}}(s) = \frac{1}{a_2 s^2 + a_1 s + 1} = \frac{1}{\frac{1}{\varpi_n^2}s^2 + \frac{2\xi}{\varpi_n}s + 1} \tag{10}$$

where $a_2, a_1 \in \mathbb{R}^*_+$, are the denominator coefficients of H^*_{cl}. ϖ_n and ξ are, respectively, the natural frequency and damping ratio. The following condition must be validated in order to obtain a real negative poles and consequently a damping ratio $\xi \geq 1$

$$a_1 \geq 2\sqrt{a_2}. \tag{11}$$

The CN is achieved by equating between the H_{cl} and the desired one H^*_{cl} to get

$$\text{CN}(s) = \frac{s^2 + 2\lambda s + \lambda^2 + \omega_{sl}^2}{\psi_r^{*2}(a_2 s^2 + a_1 s)}. \tag{12}$$

The PID CN is defined by

$$\text{PID}(s) = K_p + \frac{K_i}{s} + \frac{K_d s}{\tau s + 1} \tag{13}$$

where K_p is the coefficient of the proportional action, K_i is the coefficient of the integral action, and K_d, τ are, respectively, the coefficient of derivative action and time constant of the filter.

Lemma: The CN $\text{CN(s)} = \frac{n_2 s^2 + n_1 s + n_0}{d_2 s^2 + d_1 s}$ and the $\text{PID}(s) = K_p + \frac{K_i}{s} + \frac{K_d s}{\tau s + 1}$ are equivalent when

$$\begin{cases} K_p &= \frac{n_1 d_1 - n_0 d_2}{d_1^2} \\ K_i &= \frac{n_0}{d_1} \\ K_d &= \frac{n_2 d_1^2 - n_1 d_1 d_2 + n_0 d_2^2}{d_1^3} \\ \tau &= \frac{d_2}{d_1} \end{cases}$$

where n_2, n_1, and n_0 represent the coefficients of the numerator of the CN(s) CN and d_2 and d_1 represent the coefficients of its denominator.

The CN is calculated by equating the CLTF H_{cl} with the DCLTF H^*_{cl}, which is inherently stable. As a result, the resulting system inherits the stability characteristics of the target model.

The PID parameter can be written after applying the lemma on (12) as follows.

1) For proportional action K_p

$$K_p = \frac{2a_1\lambda - a_2(\lambda^2 + \omega_{sl}^2)}{a_1^2 \psi_r^{*2}}. \tag{14}$$

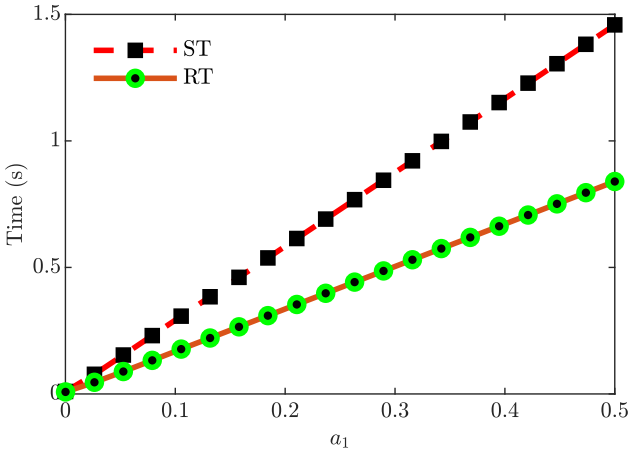

FIGURE 4. Temporal characteristic of the desired transitional regime: settling time and rise time.

2) For integral action K_i

$$K_i = \frac{(\lambda^2 + \omega_{sl}^2)}{a_1 \psi_r^{*2}}. \tag{15}$$

3) For derivative action K_d, τ

$$\begin{cases} K_d = \frac{a_1^2 - 2\lambda a_1 a_2 + (\lambda^2 + \omega_{sl}^2) a_2^2}{a_1^3 \psi_r^{*2}} \\ \tau = \frac{a_2}{a_1}. \end{cases} \tag{16}$$

The parameters of the PID CN will fluctuate in accordance with the slip speed parameter ω_{sl}, in order to establish the specified dynamics of the DCLTF. Indeed, this targeted dynamic will be integrated into the MRASF across all operational states of the IM. The subsequent section of this discourse will concentrate on the validation through simulation of the proposed PID CN utilizing the transfer function pertinent to the MRASF.

B. SIMULATION RESULTS

The DCLTF, H_{cl}^*, is meticulously formulated to fulfill the requisite performance criteria within the closed-loop control framework. Specifically, the attainment of convergence to the targeted value is facilitated by the selection of a unit static gain, whereas the mitigation of overshoot and oscillations necessitates a damping factor exceeding 1. To realize an overdamped response, the poles of H_{cl}^* are judiciously selected as distinct real negative poles.

In order to delineate the characteristics of the transient response, the parameter a_1 of H_{cl}^*, as delineated in (10), is varied across the interval [0, 0.5]. The corresponding parameter a_2 is ascertained as the boundary value that satisfies condition (11). The resultant transient performance is depicted in Fig. 4. The IM parameters are enumerated in Table 1.

Using the same interval for the parameter a_1 and considering the boundary condition in (11), the effect of the slip speed variations is analyzed within the range [0, 20] rad/s. This leads to visualize the PID parameter (14), (15), and (16)

TABLE 1. Parameters of the IM

Description	Parameter	Value
Nominal power	P_N	1 kW
Nominal voltage	U_N	3X380 V 50 Hz
Nominal current	I_N	2.5 A
Nominal speed	n_N	2780 rpm
Nominal efficiency	η_N	0.83
Nominal power coefficient	$cos\varphi_n$	0.80
Nominal torque	T_N	3.43 Nm
Stator resistance	R_s	7.2 Ω
Rotor resistance	R_r	7.2 Ω
Mutual inductance	L_m	469 mH
Stator inductance	L_s	487 mH
Rotor inductance	L_r	487 mH
Nominal inertia	J_n	0.0001 kg m^2

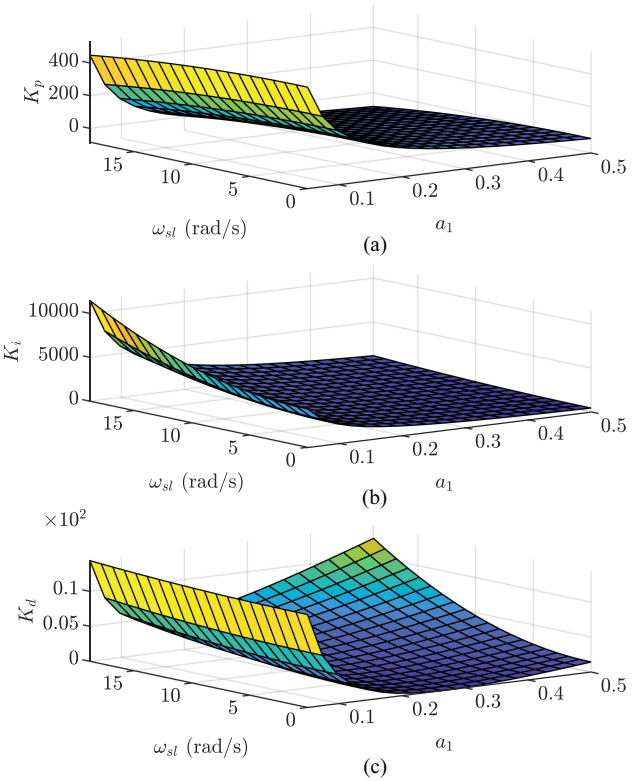

FIGURE 5. PID parameters according to desired performances and slip speed: (a) proportional action K_p, (b) integral action K_i, and (c) derivative action K_d.

as 3-D surfaces (see Fig. 5). The variations of K_p, K_i, and K_d are depicted in Fig. 5(a)–(c), respectively.

The figures reveal that for low values of a_1, K_p, and K_d exhibit minimal variations across the selected slip speed interval ω_{sl}, while K_i undergoes significant changes. Conversely, for higher values of a_1 within the same ω_{sl} range, K_p and K_d show substantial variations, whereas K_i remains nearly constant. The primary objective is to verify whether the desired system performance can be achieved for different values of ω_{sl}, given that the PID parameters are calculated accordingly. To this end, three distinct desired performances, DP_1, DP_2, and DP_3, are selected based on three predefined DCLTF (10), where the parameter values are set to $a_1 = \{0.5,\ 0.1,\ 0.05\}$.

TABLE 2. PID Parameters Based on the Chosen Desired Performances

PID \ ω_{sl}	18.84rad/s	12.56rad/s	6.28rad/s	
K_p	30	50	70	DP1
K_i	1147	752	516	
K_d	14	7	4	
τ	0.25	0.25	0.25	
K_p	210	190	167	DP2
K_i	6735	3763	2580	
K_d	12	6.2	5	
τ	0.05	0.05	0.05	
K_p	400	403	432	DP3
K_i	11470	7526	5160	
K_d	13	10	8.5	
τ	0.026	0.026	0.026	

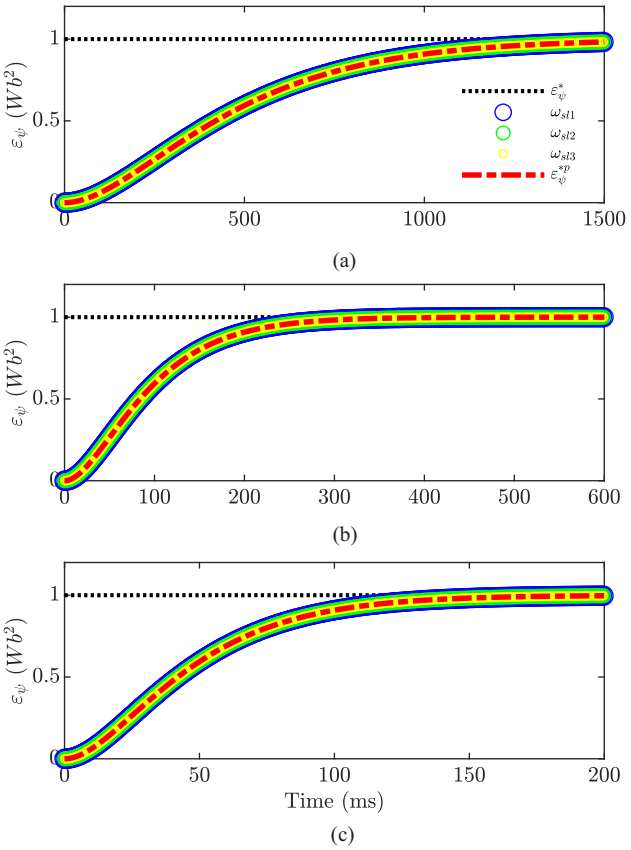

FIGURE 6. Step-response of the controlled system for different slip-speed values when: (a) DP_1 is imposed, (b) DP_2 is imposed, and (c) DP_3 is imposed.

The step response characteristics for DP_1, DP_2, and DP_3 exhibit no overshoot, with settling times of $ST_1^* = 1.45$ s, $ST_2^* = 0.29$ s, and $ST_3^* = 0.14$ s. The corresponding rise times are $RT_1^* = 0.83$ s, $RT_2^* = 0.16$ s, and $RT_3^* = 0.08$ s.

In addition, three slip speed values are selected: $\omega_{sl} = \{18.84$ rad/s, 12.56 rad/s, 6.28 rad/s$\}$. Given these parameters, and by applying (14)–(16), the corresponding PID parameters are computed and summarized in Table 2.

Fig. 6(a)–(c) clearly demonstrates that the desired performances, DP_1, DP_2, and DP_3, are successfully achieved for all selected slip speed values. Furthermore, the output signal curves in each figure closely align with the desired behavior curve, ε_ψ^{*P}, which represents the response obtained from the DCLTF under the same input conditions.

The PID parameters were calculated based on the desired performance set by a suitable choice of DCLTF. The controlled system MRASF, starting from an initial condition with a predefined slip speed, exhibits the desired behavior. Therefore, the objective of the next experimental validation will be to maintain the desired performance of the controlled system at any slip speed associated with any level of rotor speed.

IV. EXPERIMENTAL VALIDATION

The experimental validation was performed on a laboratory-built test bench including a 1-kW IM mechanically coupled to a 1-kW dc machine through a rotor speed measurement unit, which utilizes an incremental encoder with a resolution of 1024 pulses per revolution. In addition, the setup features a MicroLabBox control platform, an autotransformer, an inverter, and measurement devices (see Fig. 8). The IM parameters are listed in Table 1.

To validate the effectiveness of the proposed PID CN for the MRASF and compare its performance with a conventional PI CN, an open-loop V/F control approach is utilized (see Fig. 7). This method enables a comprehensive performance evaluation across different IM rotor speeds.

Fig. 7 illustrates the block diagram of the V/F control algorithm and the MRASF model, implemented in the MATLAB/Simulink environment. The program features two manual switches: the first one operates as a rate limiter to regulate acceleration, while the second allows switching between PI and PID CN for MRASF adaptation. The rate limiter is activated when the IM starts from zero speed and accelerates beyond 1000 r/min, ensuring smooth operation. The real-time program executed on the dSPACE MicrolabBox uses a control loop period of 150 μs. The carrier signal used for pulsewidth modulation (PWM) generation operates at 300 μs, corresponding to a switching frequency of 3.33 kHz.

The experimental tests are conducted under the assumption that the slip remains constant at 2% across all rotor speed levels when the IM is unloaded.

Test #1: The first test was conducted to validate the proposed design methodology for the PID CN in the MRASF system. Two desired closed-loop transfer functions were selected to represent the intended dynamic behavior of MRASF, defined as follows:

$$\begin{cases} H^*_{\text{cl1}} = \frac{1}{1.4\ 10^{-2}s^2+24\ 10^{-2}s+1} \\ H^*_{\text{cl2}} = \frac{1}{3.6\ 10^{-3}s^2+12\ 10^{-2}s+1} \end{cases} \tag{17}$$

where $RT_1^* = 0.51$ s, $ST_1^* = 0.92$ s, $RT_2^* = 0.2$ s, and $ST_2^* = 0.35$ s.

To validate the proposed PID CN design, it is essential to select rotor speeds below 1000 r/min to prevent activation of the rate limiter. For Test #1, two rotor speeds were chosen: 1000 and 500 r/min, corresponding to synchronous angular

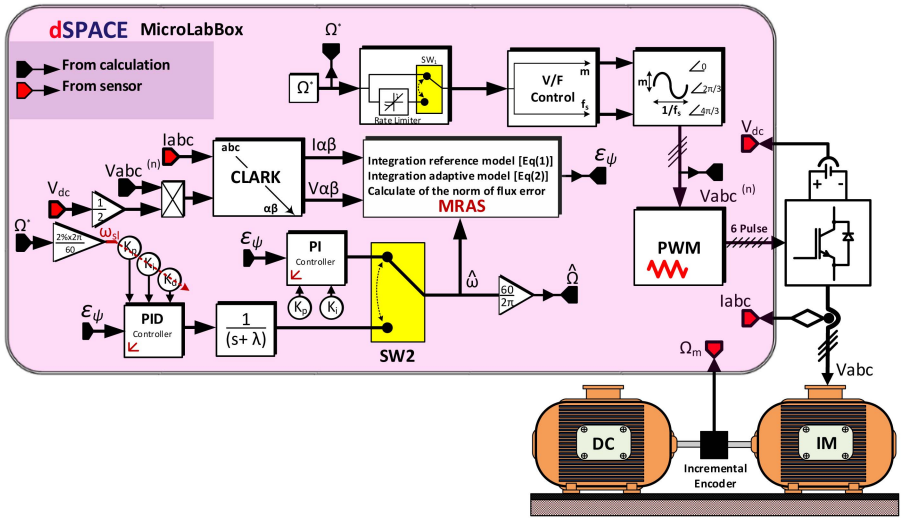

FIGURE 7. Block diagram of the V/F control algorithm and MRASF.

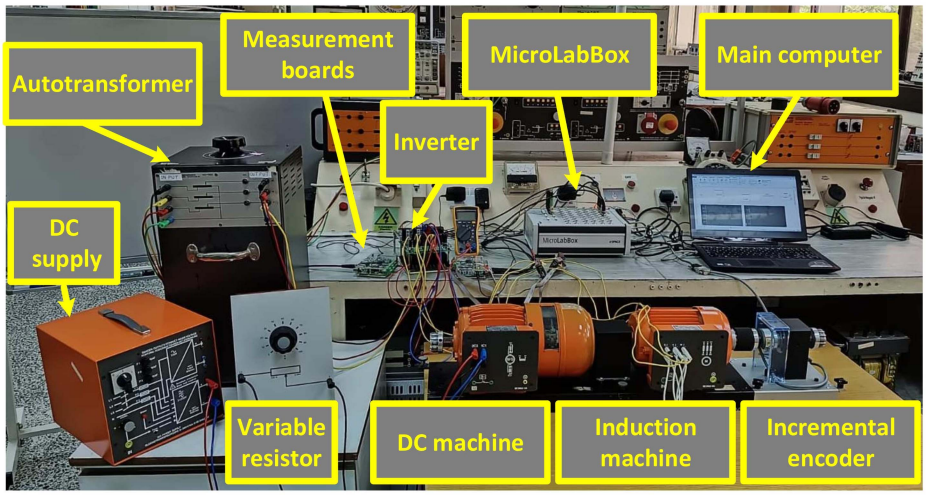

FIGURE 8. Test bench.

velocities of 104.6 rad/s and 52.3 rad/s, respectively. Assuming a 2% slip, the resulting slip speeds are 2.09 and 1.04 rad/s. The computed PID parameters from (14), (15), and (16) for the desired performances H^*_{cl1} and H^*_{cl2} are as follows.

1) $\text{PID}_1^{1000} = (380, 5100, 10, 0.05)$.
2) $\text{PID}_1^{500} = (395, 4900, 10.5, 0.05)$.
3) $\text{PID}_2^{1000} = (410, 6300, 13, 0.03)$.
4) $\text{PID}_2^{500} = (403, 5940, 11.3, 0.03)$.

Fig. 9(a) and (b) clearly illustrates that the performance of the MRASF-PID closely matches the desired performance at both speed levels.

Test #2: This validation test evaluates the proposed CN sensitivity to parameter variations. Specifically, the CN parameters derived from H^*_{cl2} were increased by 10% and 20% using reference speeds of 1000 and 500 r/min. The results of this test are represented in Fig. 10(a) and (b). As it can be noticed, the increase in parameter values led to a faster dynamic response; however, this enhancement was accompanied by overshoot levels ranging from 6% to 20% .

Test #3: Two additional experiments were conducted as part of the validation tests to assess the performance of the proposed CN during a reference change without parameter adjustments. The first test involved reducing the speed from 2000 to 1000 r/min, while the second test increased the rotor speed from 1000 to 2000 r/min. The results of these tests are shown in Fig. 11(a) and (b). Although the dynamics are similar, a noticeable tracking error exists [60 r/min in Fig. 11(a) and 40 r/min in Fig. 11(b)] between the desired estimated speed and the speed estimated by the unadjusted CN.

In all subsequent tests, the performance of MRASF was set to match that of the DCLTF H^*_{cl2}. The dynamic behavior of H^*_{cl2} closely aligns with the actual measured rotor speed. The

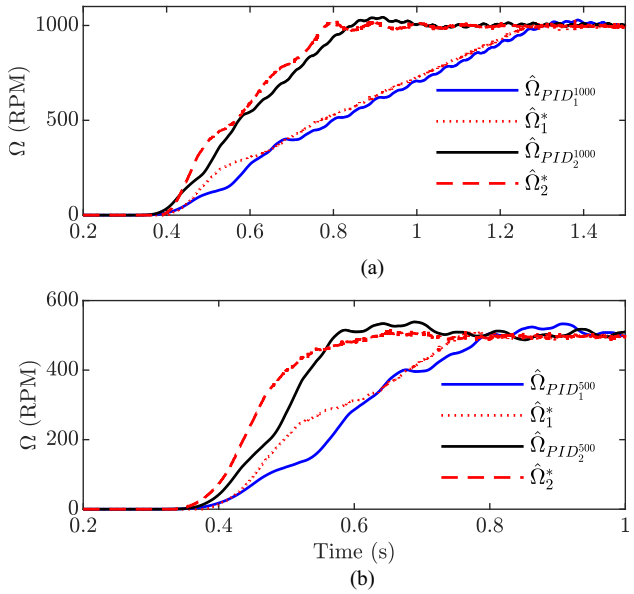

FIGURE 9. Test #1: PID validation design method for different performance and for different range of speed d. (a) 1000 r/min. (b) 500 r/min.

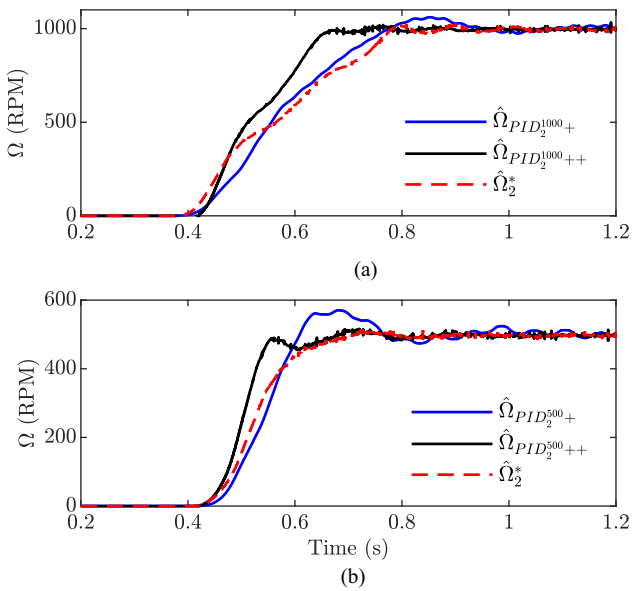

FIGURE 10. Test #2: Performances when varying PID parameters from their desired values. (a) 1000 r/min. (b) 500 r/min.

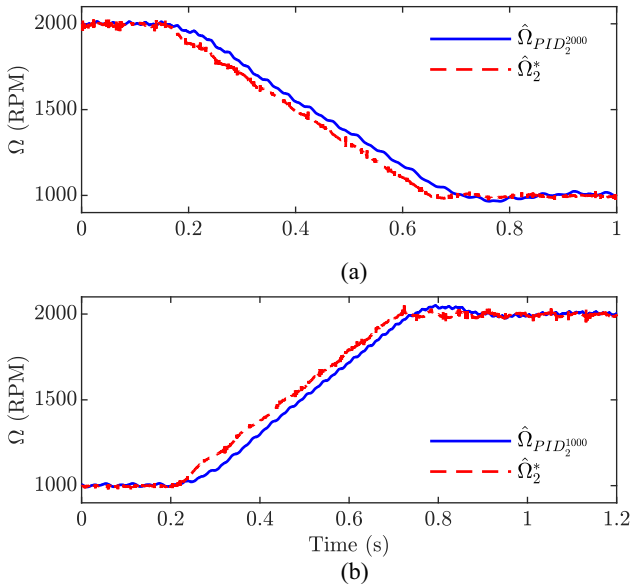

FIGURE 11. Test #3: Performances when changing the operating point without updating PID parameters. (a) 2000–1000 r/min. (b) 1000–2000 r/min.

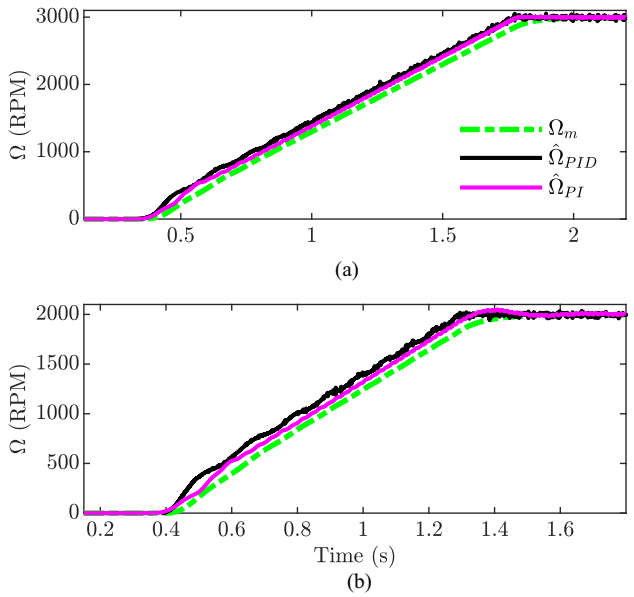

FIGURE 12. Test #4: Comparison MRASF based PI and PID at high speed. (a) 3000 r/min. (b) 2000 r/min.

PI CN parameters were fixed across the entire speed range and computed using (8), resulting in PI = (450, 5120).

Test #4: The fourth test was conducted to evaluate and compare the performance of MRASF-PID and MRASF-PI at high speeds of 3000 and 2000 r/min. To achieve this, the rate limiter was activated to minimize the starting current and ensure smooth acceleration. The objective of this test is to achieve comparable performance for MRASF using both PID and PI CN at high speeds. Establishing equivalence at higher speeds is crucial for performing an objective low-speed comparison, where the PID parameters are tuned dynamically for each slip speed ω_{sl}.

The PID parameters were computed based on H^*_{cl2} as the desired response and considering slip speeds $\omega_{sl1} = 6.28$ rad/s and $\omega_{sl2} = 4.18$ rad/s. The resulting PID values are as follows.

1) $\text{PID}^{3000} = (390, 4700, 11, 0.03)$.
2) $\text{PID}^{2000} = (392, 4300, 11, 0.03)$.

The results obtained from Test #4 for 3000 and 2000 r/min are presented in Fig. 12(a) and (b), respectively.

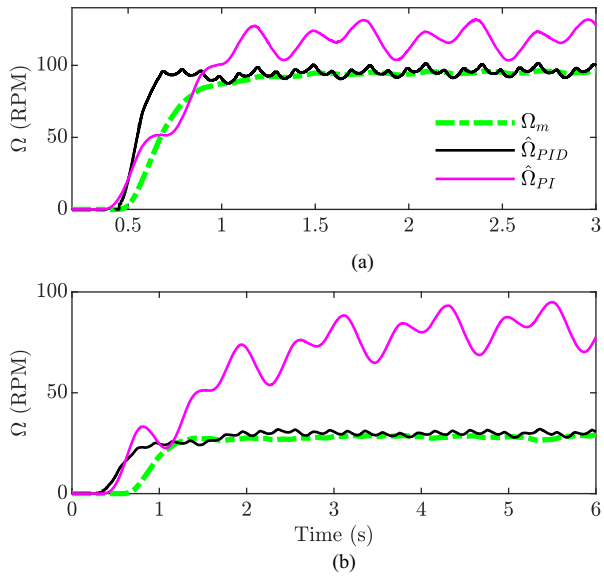

FIGURE 13. Test #5: Performance comparison of PI and PID based MRAS estimator at low speed. (a) 100 r/min. (b) 30 r/min.

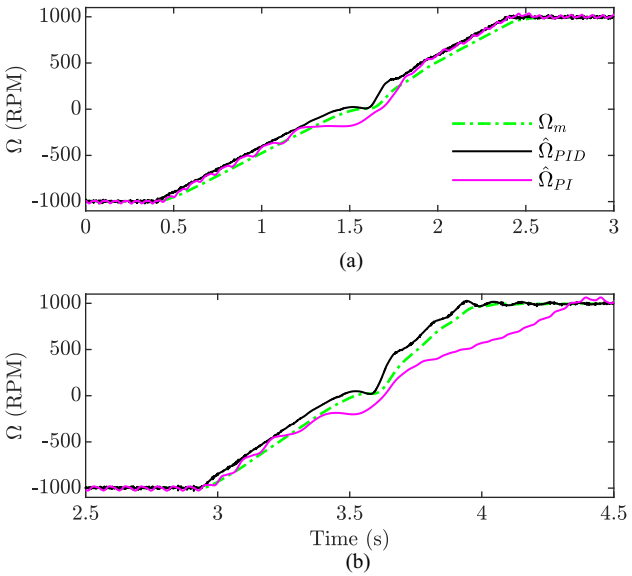

FIGURE 15. Test #7: Trapezoidal reference trajectory 1000 r/min. (a) Slope 1000 r/min/s. (b) Slope 2000 r/min/s.

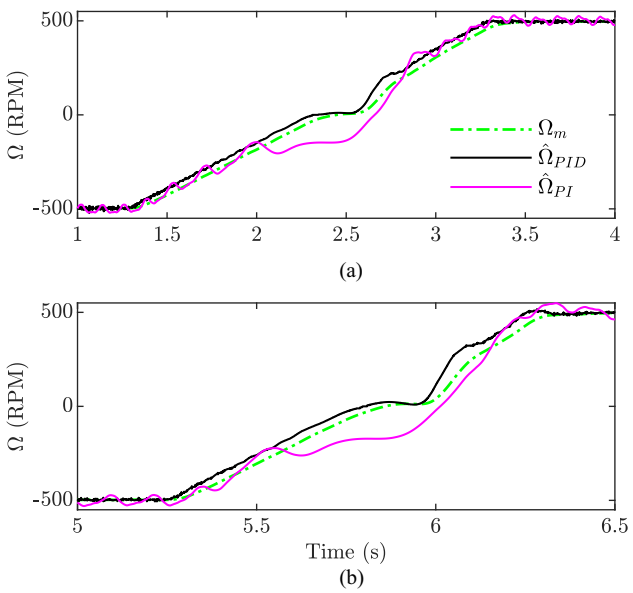

FIGURE 14. Test #6: Trapezoidal reference trajectory 500 r/min. (a) Slope 500 r/min/s. (b) Slope 1000 r/min/s.

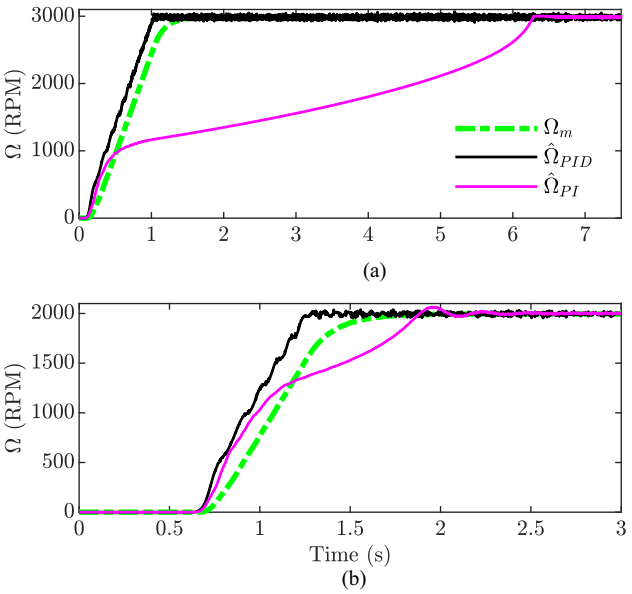

FIGURE 16. Test #8: Inertia variation. (a) 3000 r/min is imposed. b) 2000 r/min is imposed.

Test #5: The PID parameters for rotor speeds of 100 and 30 r/min are as follows.

1) $\text{PID}^{100} = (430, 4000, 14, 0.03)$.
2) $\text{PID}^{30} = (430, 3700, 14, 0.03)$.

The results shown in Fig. 13(a) and (b) clearly demonstrate that MRASF-PID outperforms MRASF-PI when operating the IM at 100 and 30 r/min, respectively. In the 100 r/min test with the PI CN, a steady-state error of 20 r/min was observed, while in the 30 r/min test, the error increased to 50 r/min. Notably, the derivative action of the PID CN improves the stability of MRASF, especially in situations where there are inaccuracies in rotor flux estimation at low speeds.

Test #6: To evaluate the system's response under dynamic conditions, several trapezoidal reference trajectories were applied to the rotor speed at different levels: 500 r/min (see Fig. 14) and 1000 r/min (see Fig. 15). The PID settings remained consistent with those used in Test #1. Fig. 14(a) presents the results for a speed slope of 500 r/min/s, while Fig. 14(b) corresponds to a 1000 r/min/s slope. Similarly, Fig. 15(a) and (b) illustrates the system response for speed slopes of 1000 and 2000 r/min/s, respectively. A comparison of all results confirms the superior performance of

MRASF-PID over MRASF-PI, particularly in terms of tracking accuracy and dynamic response.

Test #8: The final test was conducted to examine the impact of mechanical parameter variations on the dynamics of the MRAS. Specifically, a dc machine was coupled to the IM, introducing variations in system inertia.

For this test, reference speeds of 3000 and 2000 r/min were applied, the rate limiter was activated, and the PID settings remained consistent with Test #4. The obtained results are presented in Fig. 16(a) and (b), corresponding to 3000 and 2000 r/min, respectively. The findings clearly indicate that MRASF-PID outperforms MRASF-PI, primarily due to the derivative action, which enhances stability and compensates for inertia variations.

V. CONCLUSION

This manuscript presented the architecture of a PID CN conceived as an adaptive mechanism for the MRASF. The primary objective was to achieve specified dynamic and steady-state performance for rotor speed estimation in IMs. The design methodology utilized a full-order transfer function of the MRASF—which inherently depends on slip speed—and applied pole compensation and placement techniques. By matching this model with a desired closed-loop transfer function, the PID parameters were formulated as explicit mathematical expressions that relate machine characteristics, slip speed, and the coefficients of the target dynamics. To evaluate the effectiveness of the proposed MRASF-PID approach, a comprehensive set of simulation and experimental validations was conducted using open-loop V/F control of the IM. The presented simulation and experimental results clearly confirmed that the estimated speed closely follows the desired reference dynamics across a wide range of operating conditions in addition to superior accuracy and robustness compared to a conventional PI CN. These findings strongly validate the MRASF-PID design, both theoretically and practically, and demonstrate its potential for deployment in high-performance IM drives. A promising avenue for future research lies in integrating this PID-based adaptation mechanism into a closed-loop SVC framework. This integration should be accompanied by an online PID tuning mechanism responsive to real-time slip speed variations, which would further enhance the adaptability, responsiveness, and fault resilience of the system under diverse and demanding operational conditions.

VI. ACKNOWLEDGMENT

The project was funded by Kuwait Foundation for the Advancementof Sciences (KFAS) under project code: CN23-13EE-1882.

REFERENCES

[1] E. Dehghan-Azad, S. Gadoue, D. Atkinson, H. Slater, P. Barrass, and F. Blaabjerg, "Sensorless control of IM based on stator-voltage MRAS for limp-home EV applications," *IEEE Trans. Power Electron.*, vol. 33, no. 3, pp. 1911–1921, Mar. 2018.

[2] E. Zerdali and E. C. Menguc, "Novel complex-valued stator current-based MRAS estimators with different adaptation mechanisms," *IEEE Trans. Instrum. Meas.*, vol. 68, no. 10, pp. 3793–3795, Oct. 2019.

[3] A. Accetta, M. Cirrincione, M. Pucci, and G. Vitale, "Closed-loop MRAS speed observer for linear induction motor drives," *IEEE Trans. Ind. Appl.*, vol. 51, no. 3, pp. 2279–2290, May/Jun., 2015.

[4] S. Das, R. Kumar, and A. Pal, "MRAS-based speed estimation of induction motor drive utilizing machines' d- and q-circuit impedances," *IEEE Trans. Ind. Electron.*, vol. 66, no. 6, pp. 4286–4295, Jun. 2019.

[5] A. Pal, S. Das, and A. Chattopadhyay, "An improved rotor flux space vector based MRAS for field-oriented control of induction motor drives," *IEEE Trans. Power Electron.*, vol. 33, no. 6, pp. 5131–5141, Jun. 2018.

[6] H. Kojabadi, C. Liuchen, and R. Doraiswami, "A MRAS-based adaptive pseudoreduced-order flux observer for sensorless induction motor drives," *IEEE Trans. Power Electron.*, vol. 20, no. 4, pp. 930–938, Jul. 2005.

[7] M. A. Fnaiech, J. Guzinski, M. Trabelsi, A. Kouzou, M. E. Benbouzid, and K. Luksza, "MRAS-based switching linear feedback strategy for sensorless speed control of induction motor drives," *Energies*, vol. 14, no. 11, 2021, Art. no. 3083, doi: 10.3390/en14113083. [Online]. Available: https://www.mdpi.com/1996-1073/14/11/3083

[8] Y. B. Zbede, S. M. Gadoue, and D. J. Atkinson, "Model predictive MRAS estimator for sensorless induction motor drives," *IEEE Trans. Ind. Electron.*, vol. 63, no. 6, pp. 3511–3521, 2016.

[9] M. Zair and A. Hazzab, "MRAS speed sensorless vector control of induction motor drives using predictive adaptation mechanism," *Int. J. Power Electron. Drive Syst.*, vol. 9, no. 4, pp. 1523–1533, Dec. 2018, doi: 10.11591/ijpeds.v9.i4.pp1523-1533. [Online]. Available: http://iaescore.com/journals/index.php/IJPEDS/article/view/16299

[10] T. Wang, B. Wang, Y. Yu, and D. Xu, "Discrete sliding-mode-based MRAS for speed-sensorless induction motor drives in the high-speed range," *IEEE Trans. Power Electron.*, vol. 38, no. 5, pp. 5777–5790, May, 2023, doi: 10.1109/TPEL.2023.3236024.

[11] Z. Shen et al., "Sensorless control of bearingless induction motor based on fuzzy dual sliding mode MRAS," *Elect. Eng.*, vol. 107, pp. 5737–5747, 2024, doi: 10.1007/s00202-024-02835-5.

[12] M. Holakooie, M. Ojaghi, and A. Taheri, "Modified DTC of a six-phase induction motor with a second-order sliding-mode MRAS-based speed estimator," *IEEE Trans. Power Electron.*, vol. 34, no. 1, pp. 600–611, Jan. 2019.

[13] M. Comanescu and L. Xu, "Sliding-mode MRAS speed estimators for sensorless vector control of induction machine," *IEEE Trans. Ind. Electron.*, vol. 53, no. 1, pp. 146–153, Feb. 2006.

[14] J. Yan, H. Lin, Y. Feng, X. Guo, Y. Huang, and Z. Zhu, "Improved sliding mode model reference adaptive system speed observer for fuzzy control of direct-drive permanent magnet synchronous generator wind power generation system," *IET Renewable Power Gener.*, vol. 7, no. 1, pp. 28–35, 2013.

[15] M. Cirrincione, A. Accetta, M. Pucci, and G. Vitale, "MRAS speed observer for high-performance linear induction motor drives based on linear neural networks," *IEEE Trans. Power Electron.*, vol. 28, no. 1, pp. 123–134, Jan. 2013.

[16] U. Sengamalai et al., "Mitigation of circulating bearing current in induction motor drive using modified ann based MRAS for traction application," *Mathematics*, vol. 10, no. 8, 2022, Art. no. 1220, doi: 10.3390/math10081220. [Online]. Available: https://www.mdpi.com/2227-7390/10/8/1220

[17] Z. Tir, T. Orlowska-Kowalska, H. Ahmed, and A. Houari, "Adaptive high gain observer based MRAS for sensorless induction motor drives," *IEEE Trans. Ind. Electron.*, vol. 71, no. 1, pp. 271–281, Jan. 2024, doi: 10.1109/TIE.2023.3243271.

[18] L. Wang, *PID Control System Design and Automatic Tuning Using MATLAB/Simulink*. Piscataway, NJ, USA: IEEE, 2020.

[19] Z. Qi, Q. Shi, and H. Zhang, "Tuning of digital PID controllers using particle swarm optimization algorithm for a CAN-based DC motor subject to stochastic delays," *IEEE Trans. Ind. Electron.*, vol. 67, no. 7, pp. 5637–5646, Jul. 2020.

[20] B. Verma and P. K. Padhy, "Robust fine tuning of optimal PID controller with guaranteed robustness," *IEEE Trans. Ind. Electron.*, vol. 67, no. 6, pp. 4911–4920, Jun. 2020.

[21] A. Singh et al., "A digital low-dropout regulator with autotuned PID compensator and dynamic gain control for improved transient performance under process variations and aging," *IEEE Trans. Power Electron.*, vol. 35, no. 3, pp. 3242–3253, Mar. 2020.

[22] G. H. Nguyen, J. Shin, and W. Kim, "Autotuning controller for motion control system based on intelligent neural network and relay feedback approach," *IEEE/ASME Trans. Mechatron.*, vol. 20, no. 3, pp. 1138–1148, Jun. 2015.
[23] L. Wang, T. Barnes, and W. Cluett, "New frequency-domain design method for PID controllers," *IET J. Control Theory Appl.*, vol. 142, no. 4, pp. 265–271, 1995.
[24] A. S. Bazanella, L. F. A. Pereira, and A. Parraga, "A new method for PID tuning including plants without ultimate frequency," *IEEE Trans. Control Syst. Technol.*, vol. 25, no. 2, pp. 637–644, Mar. 2017.
[25] N. Killingsworth and M. Krstic, "PID tuning using extremum seeking: Online, model-free performance optimization," *IEEE Control Syst.*, vol. 26, no. 1, pp. 70–79, Feb. 2006.
[26] O. Lequin, E. Bosmans, and T. Triest, "Iterative feedback tuning of PID parameters: Comparision with classical tuning rules," *Control Eng. Pract.*, vol. 11, no. 9, pp. 1023–1033, 2003.
[27] C. Hang and K. Sin, "On-line auto tuning of PID controllers based on the cross-correlation technique," *IEEE Trans. Ind. Electron.*, vol. 38, no. 6, pp. 428–437, Dec. 1991.
[28] A. Rad, W. Lo, and K. Tsang, "Self-tuning PID controller using Newton-Raphson search method," *IEEE Trans. Ind. Electron.*, vol. 44, no. 5, pp. 717–725, Oct. 1997.
[29] M. G. Na, "Auto-tuned PID controller using a model predictive control method for the steam generator water level," *IEEE Trans. Nucl. Sci.*, vol. 48, no. 5, pp. 1664–1671, Oct. 2001.
[30] J. Guzinski and H. Abu-Rub, "Speed sensorless induction motor drive with predictive current controller," *IEEE Trans. Ind. Electron.*, vol. 60, no. 2, pp. 699–709, Feb. 2013.
[31] S. A. Davari, F. Wang, and R. M. Kennel, "Robust deadbeat control of an induction motor by stable MRAS speed and stator estimation," *IEEE Trans. Ind. Informat.*, vol. 14, no. 1, pp. 200–209, Jan. 2018.
[32] P. Cao, X. Zhang, and S. Yang, "A unified-model-based analysis of MRAS for online rotor time constant estimation in an induction motor drive," *IEEE Trans. Ind. Electron.*, vol. 64, no. 6, pp. 4361–4371, Jun. 2017.

MOHAMED AMINE FNAIECH (Senior Member, IEEE) received the bachelor of science degree in electrical-automatic engineering from the National School of Engineering of Gabes, Gabes, Tunisia, in 2004, and the master of science and doctor of philosophy degrees in electrical engineering from Picardie Jules Verne University, Amiens, France, in 2005 and 2009, respectively.

He has occupied various academic and research roles across France, Tunisia, Qatar (Texas A&M University at Qatar), and Saudi Arabia. Since the year 2018, he has been appointed as an Assistant Professor of electrical engineering with the University of Bahrain, Zallaq, Bahrain. His research interests include control systems with applications pertinent to power electronics, electrical drives, energy conversion, and the integration of renewable energies.

MOHAMED TRABELSI (Senior Member, IEEE) received the B.Sc. degree in electrical engineering from INSAT, Tunis, Tunisia in 2006, and the M.Sc. degree in automated systems and the Ph.D. degree in energy systems from INSA Lyon, Villeurbanne, France in 2006 and 2009, respectively.

From October 2009 to August 2018, he has been holding different Research positions with Qatar University, Doha, Qatar, and Texas A&M University at Qatar, Ar-Rayyan, Qatar. In September 2018, as an Associate Professor he joined the Kuwait College of Science and Technology, Kuwait City, Kuwait, where he is currently a Full Professor and Head of the Electronics and Communications Engineering Department. His research interests include control systems with applications arising in the contexts of Power electronics, energy conversion, renewable energies integration, and smart grids.

AYMAN AL-KHAZRAJI received B.Sc (1998) in Computer Engineering, M.Sc. (2000) in Mechatronics both from university of Technology Baghdad-Iraq, and Ph.D. (2008) in Systems and Control from Reims university, France. He is an assistant professor with the Dept. of Electrical and Electronics Eng. at the University of Bahrain. He has extensive experience in both academia and industry. His research interests include AI, smart cities, robotics, control systems, the Internet of Things (IoT), and renewable energy. He is the recipient of the IFAC Best Paper Award (EAAI 2014). Dr. Al-Khazraji served as a reviewer, session chair, and technical committee member for many reputable ISI and IEEE journals and conferences.

MAAMAR TALEB received the B.Sc. degree in electrotechnics from the University of Sciences and Technology of Wahran, Wahran, Algeria in 1983, the M.Sc. degree in electric power engineering from Renssealaer Polytechnic—New York, Troy, NY, USA, in 1986, and the Ph.D. degree in electrical engineering from Clarkson University—New York, Potsdam, NY, USA in 1990.

From 1990–1992, he was a Research Associate position in electrical engineering with Clarkson University. In 1992, he joined the University of Bahrain, Zallaq, Bahrain, where he is currently an Associate Professor in electrical engineering. He has authored or coauthored about 50 publications in the previous research field and published in well reputed Journals Transactions, Journals, and International Conferences. His research interests include renewable energy applications, power quality issues, power system modeling, power system dynamics and stability.

HANI VAHEDI (Senior Member, IEEE) received the Ph.D. in electrical engineering with honors from École de Technologie Superieure (ÉTS), University of Quebec, Montreal, QC, Canada, in 2016.

He is the Inventor of the PUC5 converter, holds multiple US/world patents, and transferred that technology to the industry, where he developed the first bidirectional electric vehicle dc charger based on his invention. After seven years of experience in industry as a Power Electronics Designer and Chief Scientific Officer, he joined the Delft University of Technology, Delft, The Netherlands, where he is currently an Assistant Professor with the DCE&S group, working toward the electrification of industrial processes for clean energy transition. He is also leading the 24/7 Energy Hub project with The Green Village of TU Delft, Delft, implementing a local microgrid with renewable energy resources, green Hydrogen production, and energy storage systems as the future of the clean energy transition. He has authored or coauthored more than 90 technical papers in IEEE conferences and Transactions, a book on Springer Nature, and a book chapter in Elsevier. His research interests include multilevel converter topologies, control and modulation techniques, and their applications in the electrification of industrial processes and clean energy transition, such as smart grids, renewable energy conversion, electric vehicle chargers, green hydrogen production (electrolyzers), and fuel-cell systems.

Dr. Vahedi was the recipient of the Best Ph.D. Thesis Award from ETS for the academic year of 2016–2017. He was a Co-Chair of the IEEE Industrial Electronics Society (IES) Student and Young Professionals (S&YP) committee and is currently serving as the IES Chapters Coordinator. He has been co-organizing special sessions and S&YP forums at IEEE international conferences. He is also the Associate Editor for IEEE TRANSACTIONS ON INDUSTRIAL ELECTRONICS, *Open Journal of Industrial Electronics*, and *Open Journal of Power Electronics*.